Synergistic multi-source ambient RF and thermal energy harvester for green IoT applications

Energy Reports 9 (2023) 1875–1885

Contents lists available at ScienceDirect

Energy Reports

journal homepage: www.elsevier.com/locate/egyr

Research paper

Synergistic multi-source ambient RF and thermal energy harvester for green IoT applications

Azamat Bakytbekov [a,*], Thang Q. Nguyen [a], Ge Zhang [b], Michael S. Strano [b], Khaled N. Salama [a], Atif Shamim [a]

[a] Computer, Electrical and Mathematical Science and Engineering Department, King Abdullah University of Science and Technology, Thuwal 23955, Saudi Arabia
[b] Chemical Engineering Department, Massachusetts Institute of Technology, Cambridge, MA 02139, USA

ARTICLE INFO

Article history:
Received 23 October 2022
Received in revised form 27 December 2022
Accepted 4 January 2023
Available online 9 January 2023

Keywords:
Multi-source energy harvester
RF energy harvester
Thermal energy harvester
Heatsink antenna
Self-powered IoT devices

ABSTRACT

In a future green Internet of Things (IoT) reality, billions of devices of the IoT infrastructure should be self-powered. Harvesting ambient energy to power IoT devices is an attractive solution that can extend battery life or can completely replace batteries. Considering the global applications of IoT, ubiquitous and continuous availability is an important requirement for ambient energy sources. Radio frequency (RF) energy from mobile phone towers and thermal energy from diurnal cycle temperature fluctuations are good candidates. In this study, we present a synergistic multi-source energy harvester (MSEH) comprising an RF energy harvester (RFEH) and a thermal energy harvester (TEH) integrated through a dual-function component, heatsink antenna. Both harvesters collect ambient energy 24 h a day and are not location specific. The TEH, which is in the shape of a box, collects energy using heatsinks on its sidewalls. The same heatsinks are optimized to also serve as receiving antennas of the RFEH, which collects energy from the GSM900, GSM1800, and 3G bands. Due to the synergistic integration, radiation efficiency of the antenna doubled from 40% to 80% which resulted in ∼10% increase in power conversion efficiency of the RFEH. Similarly, the average power of the TEH without heatsinks 120 μW is doubled to 240 μW for TEH with heatsinks. Field tests have shown that the outputs of the TEH and RFEH have increased 4 and 3 times compared to the independent TEH and RFEH respectively. A temperature and humidity sensor based IoT node has been successfully powered through this energy harvesting system. Overall, the MSEH can collect 3680 μWh of energy per day which is sufficient to obtain the sensors data with a time interval of 3.5 s.

1. Introduction

Today, we are going through the fourth industrial revolution in which the Internet of Things (IoT) is rapidly developing. The number of IoT devices worldwide is ∼30 billion and is expected to reach 75 billion in 2025 (Statista Research Department, 2019). This large number of IoT devices is distributed across different spatial media to serve the global ubiquitous demand for future IoT applications. Considering the abundance of IoT devices and their massive growth in the next few years, power consumption is a major concern in terms of practical implementation and environmental sustainability of the IoT. Small IoT devices are conventionally powered using rechargeable Li-ion batteries; however, the extremely large scale of the IoT infrastructure makes this solution financially and operationally impractical. Moreover, because of growing environmental concerns, the environmental impact of disposing/recycling Li-ion batteries is undesirable.

Alternatively, ambient energy can be harvested to charge low-power IoT devices. The harvested energy can be used either to extend the lifespan of batteries or to completely eliminate batteries (Zhang et al., 2022; Ramson et al., 2021; Shim et al., 2021; Ni et al., 2018; Evans et al., 2021). Solar energy is a clear candidate because it is the most powerful source of ambient energy, and the relevant industry is quite mature (Boisseau et al., 2012). However, it has certain limitations: (1) its full potential is not globally available; there are multiple places with a short sunshine duration, (2) solar panels generate energy for a maximum of only 12 h a day, (3) the efficiency of solar panels significantly deteriorates in multiple settings, such as indoor environments, hidden/buried underground areas, and places where panels are shaded or covered. Therefore, depending only on solar energy for powering IoT sensor nodes is risky. Thus, additional versatile options must be considered along with, or separately from, solar energy.

* Correspondence to: King Abdullah University of Science and Technology, Bldg. 3, seaside, fl. 2, 2247-WS07, Thuwal 23955, Saudi Arabia.
E-mail address: azamat.bakytbekov@kaust.edu.sa (A. Bakytbekov).

https://doi.org/10.1016/j.egyr.2023.01.027

Harvesting ambient energy from a single source in a solar-deprived area is unreliable because of the unpredictability of ambient energy sources. Thus, having two or more energy harvesters in one unit is a strategy that will ensure robust and continuous operation of IoT devices (Bakytbekov et al., 2020). Many proposed ambient energy harvesters are not universal, ubiquitous, and versatile and are specific to certain locations and use cases only. For example, harvesters from the vibrations of bridges (Li et al., 2021; Liu et al., 2019) and railway trains (He et al., 2020; Amoroso et al., 2015; Cho et al., 2016), vehicle tires (Yi et al., 2021; Sadeqi et al., 2015; Bowen and Arafa, 2015; Hu et al., 2011; Lee and Choi, 2014; Singh et al., 2012), and waste heat of car engines (Fathabadi, 2018; Risseh et al., 2018; Orr et al., 2016; Temizer and İlkılıç, 2016; Cheng et al., 2017). Different combinations of multi-source energy harvesters (MSEHs), such as photovoltaic–thermoelectric–kinetic (Deng et al., 2019), photovoltaic–triboelectric (raindrops) (Zheng et al., 2014; Jeon et al., 2015; Wang et al., 2017), photovoltaic–kinetic (water flow) (Zhong et al., 2016), pyroelectric–piezoelectric (Zhang et al., 2015), photovoltaic–thermoelectric (Nishijima et al., 2017; Li et al., 2014; Lee et al., 2018; Tan and Panda, 2011), and electromagnetic–kinetic (Lorenz et al., 2015) harvesters, have been reported. However, none of these studies on MSEHs show smart integration and interdependence between different harvesters where common components are shared to efficiently use space and the collected energy increases because of synergy between harvesters. Furthermore, few studies show practical real-world applications in which MSEHs power wireless sensor nodes, as in real IoT scenarios. Certain MSEHs depend on one common source, which reduces their flexibility. For example, solar–thermal (photovoltaic–thermoelectric) energy harvesters (Nishijima et al., 2017; Li et al., 2014) simultaneously collect solar light and solar heat. Hence, the absence of sun radiation shuts these harvesters down. Combined harvesting from radio frequency (RF) and thermal sources has been presented in Guo et al. (2020) and Virili et al. (2015). In these studies, static-type thermal energy harvesters (TEHs) (waste heat source-dependent), which are simple off-the-shelf single thermoelectric generators (TEGs), were used to bias the rectifier diodes to enhance the power conversion efficiency (PCE). The RF energy harvesters (RFEHs) in both works are simple, single-band 2.4 GHz rectennas. Thus, they have limited ability to collect RF energy.

We address the abovementioned limitations by presenting an ambient MSEH that collects RF energy and thermal energy (transient-type, from diurnal temperature fluctuations). Both the RFEH and TEH can work in solar-deprived areas, and unlike solar energy harvesters, both are available 24 h a day. These harvesters do not depend on one common source. In the absence of either the RFEH or TEH, the remaining harvester can compensate and ensure continuous operation of IoT devices. Moreover, both the RFEH and TEH are not location specific; they can work in any environment with mobile phone wireless signal and diurnal temperature fluctuations, which are reported in most outdoor and indoor environments. The TEH operates using carefully selected phase change material (PCM) and TEGs. In this study, the TEH is in the shape of a box, and has evolved from a simple one-dimensional (1D) design (TEG on top face only) to a three-dimensional (3D) design (TEGs on top and four side faces of the box) to take advantage of the heat leaked through the sidewalls. Its performance was further enhanced by increasing the heat transfer between the PCM and the ambient environment through custom-designed heatsinks on the sidewalls of the TEH box. The heatsinks was designed via computational fluid dynamics (CFD) simulations in Ansys Fluent. At the same time, the heatsinks were co-optimized for electromagnetic (EM) performance in the Ansys HFSS simulator to act as the receiving antennas for the RFEH to collect energy from the GSM 900 MHz, GMS 1800 MHz, and 3G 2100 MHz bands. The radiation efficiency of the RFEH antenna doubled from 40% to 80% with the placement of the heatsink fins, which resulted in 10% increase in PCE of the RFEH. Similarly, simulations have shown that the average output power of the TEH with heatsinks is 240 μW, which is twice that of the TEH without heatsinks 120 μW. The energy collected per day during the field tests from the TEH and RFEH was improved by 4 and 3 times, respectively. Overall, the MSEH can collect 3680 μWh energy per day. Real-world IoT application was demonstrated by completely powering an environmental sensor using the MSEH. Temperature and humidity data can be acquired through Bluetooth Low Energy (BLE) communication with time interval of 3.5 s by combining the power of both harvesters.

2. Design of the multi-source ambient energy harvester

2.1. Design evolution of the TEH

The proposed transient-type TEH differs from the conventional static-type TEH, which generates energy from a waste heat source. In static-type TEHs, one cold end and one hot end are required across the TEGs to convert the temperature difference into electrical energy. The primary disadvantage of static TEHs is that they are location specific; i.e., they depend on certain applications that release waste heat, such as machines. This disadvantage of static TEHs significantly limits their future application for powering randomly distributed IoT sensors in the environment. Instead, proposed transient-type TEH converts temperature fluctuations in the environment (diurnal temperature variations) into a temperature gradient across TEGs using the high latent heat of a PCM (Cottrill et al., 2019). Latent heat is the energy released or absorbed during the phase transition process, which occurs at constant temperature. Because a large amount of energy is required for the phase transition of a PCM, it mostly exists at its phase transition temperature, thus providing constant temperature to one end of a TEG. The opposite end of the TEG follows the diurnal temperature fluctuation. Therefore, a PCM with a phase transition temperature close to the midpoint of the day and night temperature extremes must be used. In summary, the transient-type TEH is more universal and versatile than static TEHs because it can operate in any environment with natural temperature fluctuations (almost all outdoor and most indoor settings) with an appropriate PCM.

Fig. 1(a–b) shows the basic structure of the transient TEH; a container (gray) is filled with a PCM (blue). The container is sealed with an aluminum (Al) lid (orange), which prevents leakage when the PCM is in the liquid state. Al is selected because of its good thermal conductivity ($k = 229$ W m^{-1} K^{-1}). As shown by the cross-sectional view of the TEH in Fig. 1(b), the TEGs are placed on top of the Al lid. The bottom side of each TEG follows the phase transition temperature of the PCM, whereas the top side follows the ambient environment temperature fluctuations. Another Al sheet is placed on top of the TEGs as a cover; this is not shown in Fig. 1 (which only shows the inner parts). The analytical model of the TEH showed that the power output is proportional to the thermal effusivity e of the incorporated PCM:

$$e = \sqrt{k\rho C_p}, \tag{1}$$

where k, ρ, and C_p are the thermal conductivity, density, and heat capacity, respectively. Eicosane (E) is selected as the PCM because of its high heat capacity ($C_p = 5000$ J kg^{-1} K^{-1}) and its phase transition temperature (37 °C), which is close to the midpoint between the day and night extremes in Saudi Arabia (25 °C and 50 °C, respectively). On the basis of (1), the thermal conductivity of the PCM can be increased to enhance the power output of the

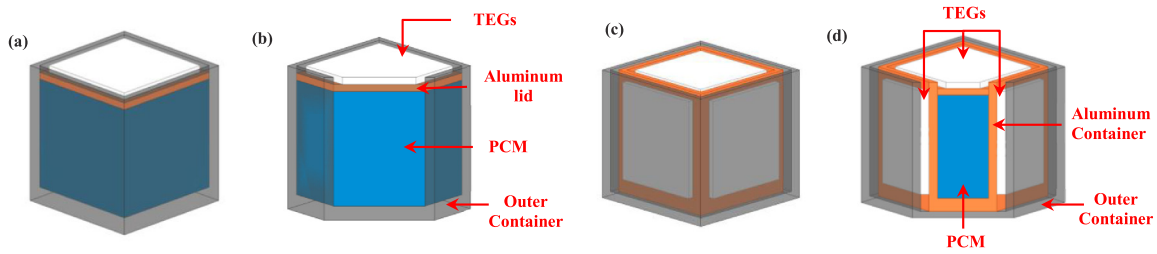

Fig. 1. (a) Isometric view of the 1D TEH (b) Cross-sectional view of the 1D TEH (c) Isometric view of the 3D TEH (d) Cross-sectional view of the 3D TEH . (For interpretation of the references to color in this figure legend, the reader is referred to the web version of this article.)

Table 1
Thermal properties of materials.

	PCM	TEG	Al	ABS
k (W m^{-1} K^{-1})	1	1	229	0.258
C_p (J kg $^{-1}$ K^{-1})	5000	500	898	1720
ρ (kg m^{-3})	930	3120	2710	1040

TEH. Therefore, nickel (Ni) foam with a thermal conductivity of 106 W m^{-1} K^{-1} is used to increase the total thermal conductivity of the E–Ni mixture. This design reflects a 1D thinking, where only the top side of the TEH is used to generate electrical energy, which leads to severe heat loss through the sidewalls. This layout can be improved by considering 3D heat transfer, i.e., by converting the heat from the sidewalls into electrical energy. Thus, a 3D design is developed, where TEGs are placed on multiple sides of the TEH: the top and the four sidewalls. As shown in Fig. 1(c–d), for the 3D design, an Al container (orange) is used to accommodate the PCM (blue). The TEGs are sandwiched between the Al container and the outer container on all five sides of the box. In this manner, the inner and outer faces of the TEGs experience the temperatures of the inner PCM and the outer environment, respectively. These additional TEGs can use the heat leaked through the sidewalls of the box, which is wasted in the 1D design. This evolution of the TEH from a 1D design to a 3D design is expected to increase the output power of the TEH. A 3D transient heat transfer simulation that realistically shows the physical device is conducted in the CFD simulator Ansys Fluent for both the 1D and 3D designs to confirm the utility of the latter.

The thermal properties of each component of the TEH are assigned based on the materials: PCM (mixture of E and Ni), aluminum box (Al), outer plastic box (ABS–acrylonitrile butadiene styrene), and TEGs. All material properties are summarized in Table 1.

All properties are assumed constant with respect to temperature because the temperature range is relatively small. Boundary conditions are set for each external surface to account for the convective and radiative heat transfers between the TEH and ambient environment. The heat transfer coefficient on flat surfaces is assumed to be 10 W m^{-2} K^{-1}. The emissivity of the external surfaces is set to 0.1 because of the light color of the experimental device. A contact heat conductance of 50 W m^{-2} K^{-1} is assigned to both sides of each TEG to account for the imperfect interfacial contact.

The time evolution of temperature distribution is solved at an experimentally measured periodic ambient temperature as the boundary condition (Fig. 2(a)), and a uniform temperature of 28.5 °C across the whole device is set as the initial condition. The heat transfer follows:

$$\frac{\partial T}{\partial t} = \alpha[\frac{\partial^2 T}{\partial x^2} + \frac{\partial^2 T}{\partial y^2} + \frac{\partial^2 T}{\partial z^2}], \tag{2}$$

where $\alpha = k/\rho C_p$ is thermal diffusivity.

After the solution is obtained, the output power of the harvester is calculated as the product of the heat flux and efficiency, which are both derived from the temperature difference between the two sides of each TEG.

$$P = A\frac{T_H - T_C}{R_{TE}}\eta, \tag{3}$$

$$\eta = \left(1 - \frac{T_C}{T_H}\right)\frac{\sqrt{1+ZT} - 1}{\sqrt{1+ZT} + \frac{T_C}{T_H}}. \tag{4}$$

where P is the output power of a TEG; A is the area of the TEG; T_H and T_C are the average temperatures of the hot and cold sides of the TEG, respectively; R_{TE} is the thermal resistance of the TEG; and η is the thermal-to-electrical energy conversion efficiency, which is a function of temperature gradient, as calculated in (4). ZT is the thermoelectric figure of merit, which is assumed to be 1 for the standard commercial Bi_2Te_3 TEG used in this work. We simplify the simulation of TEGs by ignoring the change in heat flux due to the Seebeck effect because the thermal-to-electric energy conversion efficiency is considerably smaller than 1% under the simulated conditions. Fig. 2(b–c) shows a snapshot of the simulated temperature distribution of 1D and 3D devices when the ambient temperature reaches a peak value of 53 °C. The basic design, with only one TEG on top of the TEH, has a smaller temperature difference across the device, as shown in Fig. 2(b). This is possible because of its inferior heat exchange with the environment and severe heat leakage from the sidewalls. With the four TEGs on the sides in the improved design, heat via the sidewalls is utilized to generate power. Each additional TEG has a temperature drop of a similar magnitude as the top TEG, as shown in Fig. 2(d–e). Therefore, the 3D design can produce five times as much power as the basic 1D design. As shown in Fig. 2(f–g), the average harvested power values of the 1D TEH and 3D TEH are 23 and 120 μW, respectively. This enhancement of 5.2 times shows the effectiveness of the TEH evolution from the 1D design to the 3D design.

2.2. Design of the RFEH

RF energy can be considered as an ambient source of energy in any human living environment. With the rapid development of wireless technologies in recent years, many standards now occupy the RF spectrum. Thus, more EM energy is available in the ambient environment, which makes RF sources good candidates for energy harvesting. However, the available ambient RF energy level is relatively low because the power of each wireless standard is restricted by exposure safety regulations. Therefore, simultaneous energy collection from several bands can increase the output power of the RFEH (Bakytbekov et al., 2018). RF power measurement in a university campus area demonstrated that the most powerful bands are GSM 900 MHz, GSM 1800 MHz, and 3G 2100 MHz (Bakytbekov and Shamim, 2019). Thus, the RFEH in

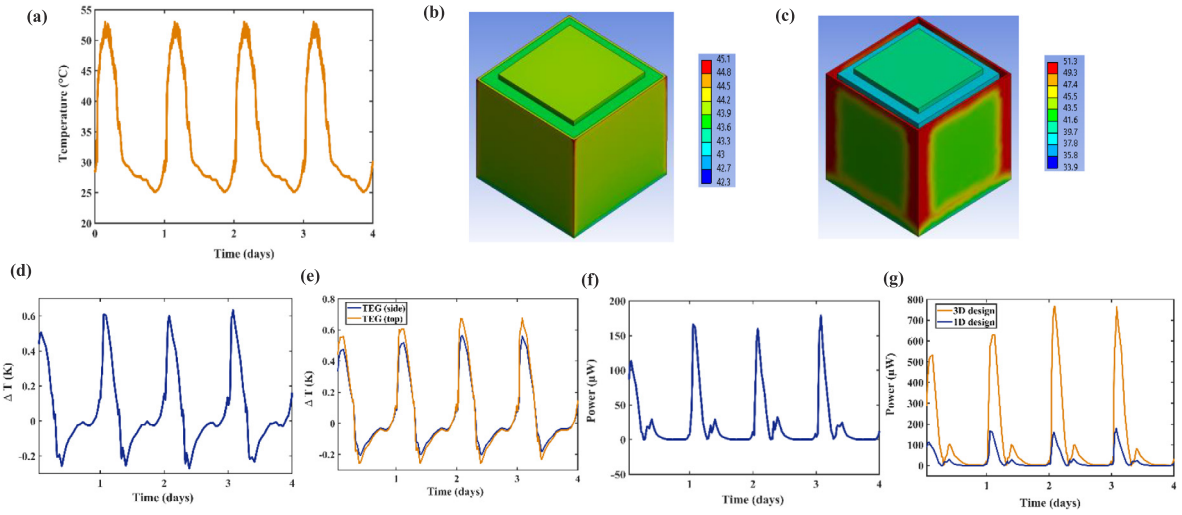

Fig. 2. (a) Measured ambient temperature fluctuations (b) Temperature distribution on the 1D design (c) Temperature distribution on the 3D design (d) Temperature difference across the TEG of the 1D design (e) Temperature difference across the TEGs of the 3D design (f) Collected power of the 1D design (g) Collected power of the 3D design.

this work is designed to simultaneously collect energy from these three bands.

The RFEH is a combination of a receiving antenna and a rectifier circuit (converts AC to DC) connected through an impedance matching network, as shown in Fig. 3(a). The output power and the PCE of the RFEH system can be calculated by (5) and (6):

$$P_{out} = P_{DC} = (V_{DC})^2/R_L \tag{5}$$

$$\eta\,(PCE) = \frac{P_{out}}{P_{in}} \tag{6}$$

where V_{DC} is output DC voltage measured across the load resistor R_L and P_{in} is the input power captured by the receiving antenna. Also, the PCE of the RFEH system can be characterized as a chain of efficiencies of individual components as given in (7):

$$\eta\,(PCE) = \eta_A \cdot \eta_{MN} \cdot \eta_0 \cdot \eta_L \tag{7}$$

where η_A and η_{MN} are the efficiencies of the receiving antenna and the impedance matching network respectively. Diode's nonlinear conversion efficiency is denoted as η_0, and η_L represents the efficiency of the power transfer to the load. Therefore, during the design process it is important to maximize the efficiency of each component to achieve the best possible PCE of the whole system.

The straightforward approach of combining the RFEH and TEH is to install the receiving antenna of the RFEH on the sidewalls of the outer container of the TEH. To proceed with this approach, the RF characterization of the TEH body in terms of the dielectric constant and loss tangent must be conducted. The identified electrical properties of the TEH body must be used in Ansys HFSS during the antenna design process. This step is important because the antenna operates in close proximity to the body of the TEH, thereby affecting the performance of the antenna.

The body of the TEH consists of four layers of the materials presented in Section 2.1 and Fig. 1(d). Al and ABS have universally known electrical properties, but TEGs and PCM (E–Ni mixture) have never been characterized in the required GHz range. Because the PCM is placed inside the Al container, the PCM model in Ansys HFSS is simplified as that of bulk Ni. This assumption is proven true through simulations and then through measurements. Because TEGs have a complex multi-material structure, their electrical properties are extracted through microwave measurements by assuming each TEG as a homogeneous black box. The measurement results presented in Fig. 3(b–c) indicate that the electrical properties of TEGs are frequency dependent. Moreover, TEGs are quite lossy in the required GHz range, as shown in Fig. 3(c).

The receiving antenna of the RFEH must be designed without a ground plane to limit the addition of extra components and to avoid complicated feeding issues. Therefore, a differential wire antenna with two arms is placed on two adjacent side faces of the TEH box. Because triple-band RF energy harvesting is required, this antenna must be a triple-band antenna operating at the 900, 1800, and 2100 MHz frequency bands. The concept of fractals is adopted for each arm to design the triple-band differential antenna. Fractals are self-repetitive structures across different scales, and they enable convenience in designing wideband or multiband antennas (Balanis, 2005). Cantor fractals (shown in Fig. 3(d)) are used in the antenna design since it has relatively simple structure and can serve as a baseplate for heatsink fins later in the design process. As shown in Fig. 3(d) the rectangular shapes are divided in three, and the middle one is deleted per iteration. A triple-band Cantor fractal antenna is smartly designed so that each iteration of the fractal structure is responsible for one frequency band. This allows to independently tune the antenna for one of the frequency bands without disturbing much the performance of the others. Thus, three iterations are required to obtain triple-band antenna performance and the evolution of the Cantor fractal antenna is displayed in Fig. 3(e–g). The length of the rectangle of the first iteration (Fig. 3(e)) is calculated to be 82 mm which represents the wavelength at 1 GHz on the ABS substrate. The longer current paths equivalent to 1.8 GHz and 0.9 GHz wavelengths are attained with the 2nd and 3rd iterations of the Cantor fractal, as shown in Fig. 3(f, g). Since the ultimate goal of the design is to achieve a heatsink antenna that improves the heat transfer (thus the output power of the TEH) the baseplates of the heatsink, that are represented as the Cantor fractal rectangles, must cover as much area as possible on the surface of 80 mm × 80 mm TEGs on the sidewalls of the TEH (shown in Fig. 1(c, d)). With more parametric optimization on Ansys HFSS, the dimensions of the Cantor fractal rectangles as well as the small separations between the rectangles have been designed in a way that maximum area coverage is achieved on the side faces of the TEH. In general, fractal antennas show efficient space-filling properties that can be positively used in our case to concentrate the antenna elements on the required area. The rectangular shapes of the Cantor fractal effectively fill the available

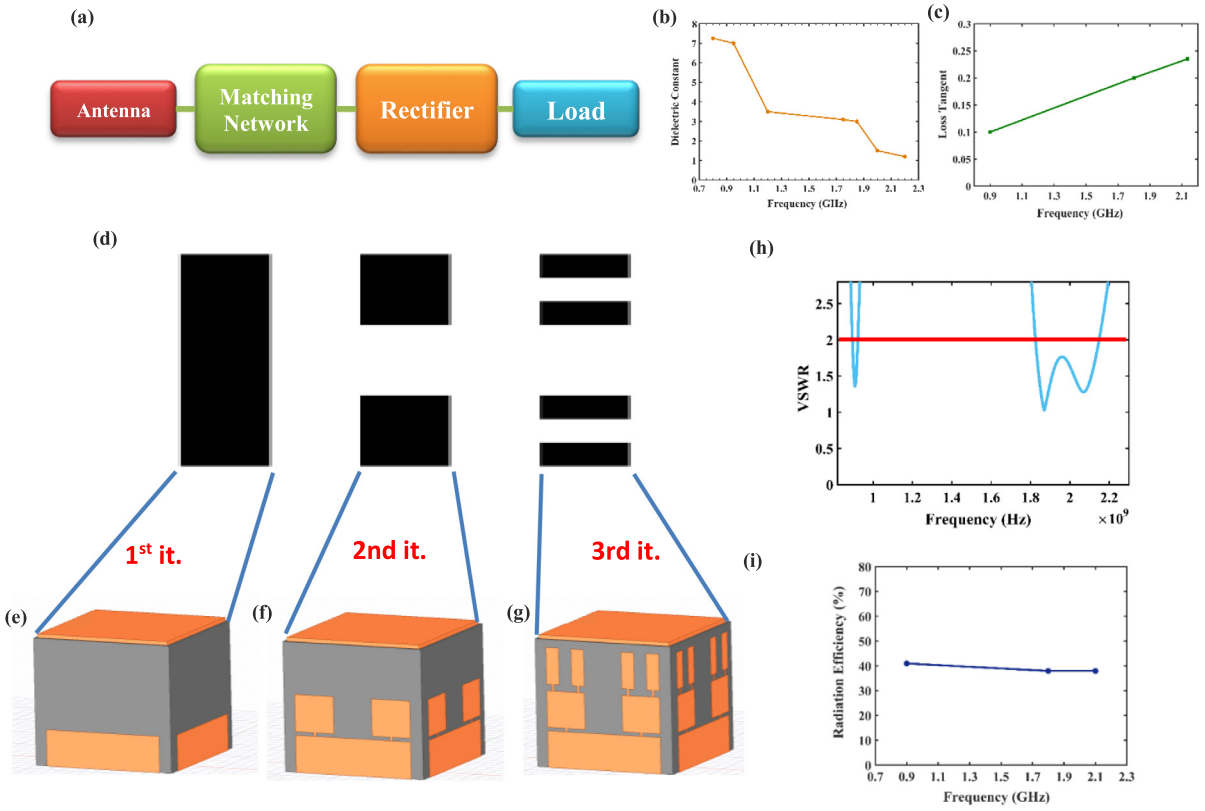

Fig. 3. (a) Block diagram of the RFEH (b) Measured dielectric constant of the TEGs as a function of frequency (c) Measured loss tangent of the TEGs as a function of frequency (d) Cantor fractal structure (e) Cantor fractal antenna with 1st iteration (f) Cantor fractal antenna with 2nd iteration (g) Cantor fractal antenna with 3rd iteration (h) VSWR of the 2D flat Cantor fractal antenna (i) Radiation efficiency of the 2D flat antenna.

space on the surface the TEH for further fin placement, compared to the straight-line shaped classic wire antennas (Balanis, 2005).

Fig. 3(h) shows the voltage standing wave ratio (VSWR) of the designed 2D Cantor fractal antenna where values below 2 shows a good impedance matching of the antenna (equivalent to S_{11} below -10 dB). For an omnidirectional radiation pattern of the RFEH antenna, which is important for all-around harvesting, one more antenna is placed on the two remaining adjacent side faces of the TEH. Thus, a total of two RFEHs are integrated in the design.

This thin metallic antenna directly placed on the sidewalls of the TEH has a low radiation efficiency, as shown in Fig. 3(i). Its radiation efficiency of ∼40% is significantly lower than the expected efficiency value of a metallic antenna. This large drop in antenna radiation efficiency is caused by the body of the TEH, which has extremely lossy components, such as the TEGs, as shown in Fig. 3(c). This problem will be tackled in the next section through a design of a 3D heatsink antenna and synergistic MSEH.

Captured RF energy by the antenna must be converted into DC power and thus a rectifier circuit is required. Series single diode rectifier topology is designed for this work since it is the best candidate for the ambient RF energy harvesting application due to its high sensitivity and minimum diode loss. A Schottky diode SMS 7630–079 from Skyworks, is used since it has low turn-on voltage as well as the minimum power consumption. Nonlinear SPICE diode parameters from the datasheet was used in Keysight ADS to model the diode in circuit simulations. The input impedance of the diode has been obtained from the simulations for all three frequencies of interest. To provide maximum power transmission from the antenna to the rectifier circuit, an impedance matching network, that matches the complex input impedance of the diode to the 50 Ω antenna impedance, must be designed. However, it is a challenging task since the input impedance of the diode is a function of frequency, input power and load condition. Thus, the load resistor of 10 kΩ is selected to achieve maximum PCE. Also, input power level was fixed to -20 dBm which is a reasonable average value for ambient environment. To minimize the insertion loss of the matching network as well as the number of components, one triple-band matching network that covers all three frequency bands simultaneously has been designed on Rogers RT/duroid 5880 substrate (tan $\delta = 0.0009$). As shown in Fig. 4(a), the network consists on an inductor, one short stub and two radial stubs whose dimensions are optimized on ADS to work at all three frequencies in parallel. The reflection coefficient of the rectifier circuit with the triple-band matching network is presented in Fig. 4(b), where decent match at all three frequencies has been achieved.

2.3. Synergistic multi-source ambient energy harvester

The use of a dual-function component, such as a heatsink antenna, is proposed to enhance the performance of the RFEH and the TEH simultaneously and to make the design of the MSEH more monolithically integrated and synergistic.

Originally, a heatsink is a component that enhances the heat transfer between two media by increasing the convection-active surface area, as shown in Fig. 5 (Incropera, 2007). The optimization of the finned surface dimensions, namely, the fin length (L), fin thickness (t), fin spacing (S), and fin orientation, is studied in Ansys Fluent simulations for our specific climate conditions to achieve the best heat transfer performance (Bakytbekov et al., 2022).

At the same time, these metallic structures can be tuned and optimized to work as receiving antennas of the RFEH to achieve smart integration between the two harvesters. These fins,

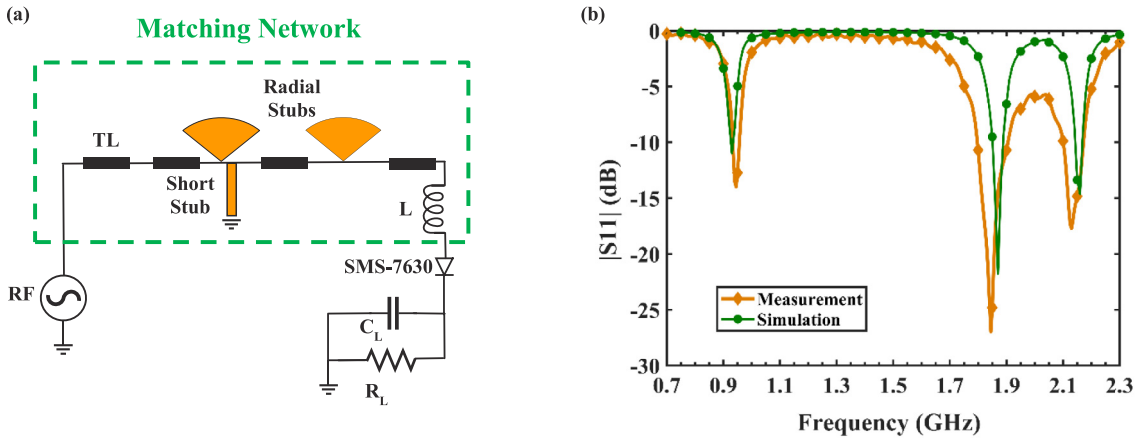

Fig. 4. (a) Schematic diagram of the triple-band matching network and the rectifier circuit (b) Reflection coefficient of the rectifier with the triple-band matching network.

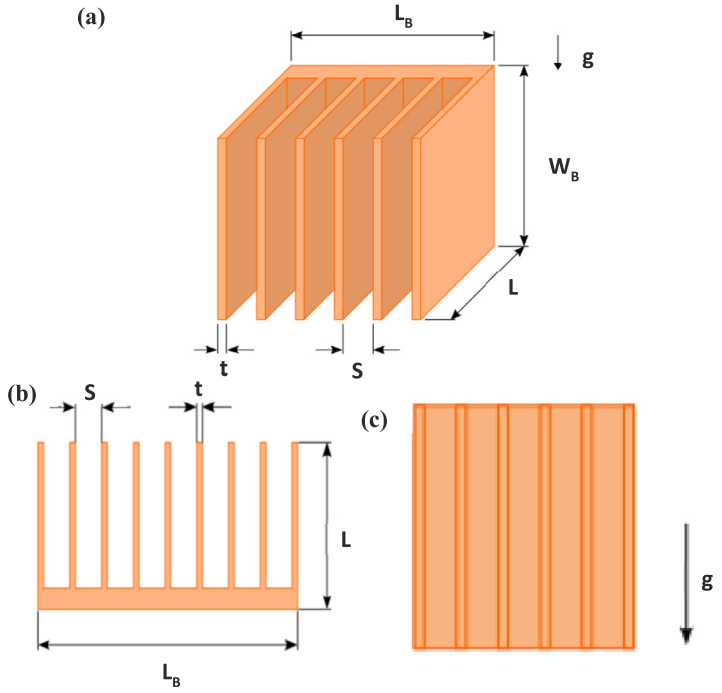

Fig. 5. (a) Isometric view of a vertically-oriented heatsink (b) Top view of a heatsink (c) Side view of a heatsink.

whose dimensions are extracted from the optimal heat transfer simulations, are integrated into a 2D flat Cantor fractal antenna to form a 3D heatsink antenna. The rectangular parts of the Cantor fractal are used as a baseplate for the heatsink. The fractal and fin dimensions are co-optimized and co-adjusted in Ansys HFSS and Ansys Fluent in parallel to achieve a balanced performance, i.e., optimal heat transfer performance and optimal antenna radiation performance (Bakytbekov et al., 2022). Fig. 6(a) shows the transformation of the 2D flat antenna into a dual-function 3D heatsink antenna. The 3D heatsink antenna enhances the performance of the RFEH by improving the antenna radiation efficiency of the 2D flat antenna from the previous design, which is severely affected by the lossy body of the TEH, as shown in Fig. 3(i). When the fins are integrated into the 2D flat antenna, the electric fields are less confined in the lossy body of the TEH, rather dominated by the surrounding medium with a lower loss tangent. As shown in Fig. 6(b), the antenna radiation efficiency doubles from 40% to 80% at all three frequency bands when the 2D flat antenna is transformed into the 3D heatsink antenna, despite the presence of the same lossy TEH body. Thus, the gain of the antenna for all three frequencies are enhanced and shown in Table 2.

Table 2
Gain of the heatsink antenna.

Frequency (MHz)	Gain (dB)
900	3.8
1800	4
2100	5.3

Fig. 6(c) shows an efficiency comparison of the RFEH with the 2D flat antenna and the 3D heatsink antenna for different input power levels when the RFEH harvests from all three frequencies simultaneously. The total PCE of the RFEH for all three frequencies

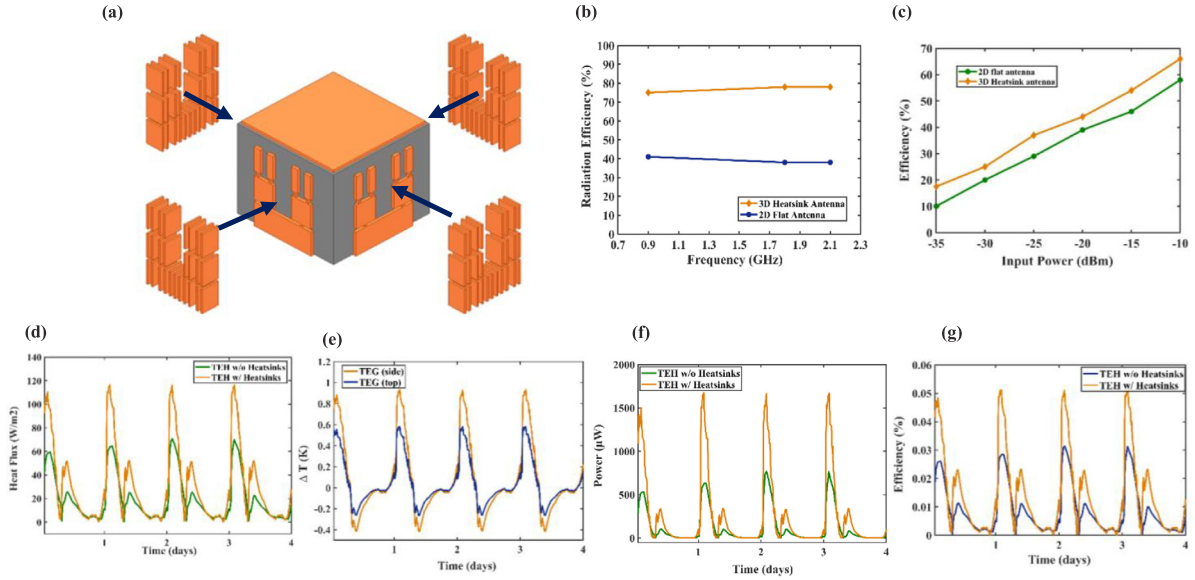

Fig. 6. (a) MSEH with the 3D heatsink antenna (b) Radiation efficiency of the 2D flat antenna and 3D heatsink antenna on the body of the TEH (c) Efficiency of the RFEH with the 2D flat antenna and the 3D heatsink antenna (d) Heat flux on the sidewalls of the TEH w/ and w/o the heatsink antennas (e) Temperature difference across the TEG of the TEH with the heatsink antennas (f) Collected power of the TEH with the heatsink antennas (g) Thermal to electrical conversion efficiency of the TEGs on the sidewalls for the TEH w/ and w/o the heatsink antennas.

is enhanced by ∼10% when the heatsink fins are integrated, highlighting the effect of the 3D heatsink antenna on the performance of the RFEH.

From the heat transfer perspective, the heatsinks increase the convection-active surface area and thus improve the heat transfer. Heatsinks are attached to the four sidewalls of the TEH based on the 3D heatsink antenna design shown in Fig. 6(a). Vertically oriented heatsink fins are preferred because of their alignment with the flow of natural convection because of gravity. The presence of the heatsinks on top of the TEH has a negligible effect on the performance of the TEH, as confirmed by the simulation. Thus, only the heatsinks on the sidewalls are examined. The addition of the heatsink fins to the sidewalls improves the heat exchange between the TEH and the environment. The heat flux through the side TEGs is nearly doubled for the TEH with heatsinks compared with the design without heatsinks (Fig. 6(d)). Consequently, the temperature drop across the side TEGs is significantly enhanced, as shown in Fig. 6(e). Fig. 6(f) shows the comparison of the output power of the TEHs with and without heatsinks, where the TEH with heatsinks demonstrate considerable increase relative to that of the TEH without heatsinks. The average output power over four days of the TEH with heatsinks is 240 μW, which is twice that of the TEH without heatsinks (120 μW). The thermal-to-electrical energy conversion efficiency is proportionally enhanced when the heatsink antennas are added, as shown in Fig. 6(g).

3. Fabrication of the multi-source ambient energy harvester

The inner container, made of Al with dimensions of 100 mm × 100 mm × 100 mm and a wall thickness of 5 mm, is manufactured using a computer numerical control (CNC) machine. This Al container is filled with a porous Ni mesh, as shown in Fig. 7(a). Then, 99% melted E is poured inside the container. An Al lid is placed on top of the container, which is properly sealed to avoid E leakage. The outer container, composed of ABS plastic with dimensions of 120 mm × 120 mm × 105 mm and a wall thickness of 5 mm, is 3D-printed using a Raise3D printer (Fig. 7(b)). The inner container is placed inside the outer container as shown in Fig. 7(c), with a 5 mm gap between them. These gaps are filled with four TEGs connected in series; therefore, a total of 20 TEGs are distributed across the five sides. Thermal paste is applied to both sides of the TEGs to ensure high thermal conductivity between the TEGs' and containers' walls. Finally, the Al lid is placed on top of the TEH as a cover (Fig. 7(d)).

The heatsink antennas, which are components of both the TEH and the RFEH, are fabricated from Al using the CNC machine (Fig. 7(e)). Al is selected because of its decent thermal and electrical conductivity, low cost, and easy manufacturability. Four heatsinks are fabricated for the four sidewalls of the TEH to improve heat transfer and to operate as two receiving antennas of the RFEH. The heatsink antennas are attached to the TEH box, as shown in Fig. 7(f).

The rectifier circuit and triple-band matching network are fabricated on a Rogers RT/duroid 5880 substrate, which has a dielectric constant of 2.2 and loss tangent of 0.0009. The circuit board is manufactured on an LPKF prototyping machine. The circuit components, namely, diode (SMS 7630–079), inductor (18 nH), capacitor (1000 pF) and load resistor (10 kΩ), are soldered according to the layout design. The rectifier circuit with the matching network is shown in Fig. 7(g).

4. Field testing

Two versions of the TEH, one with heatsinks and another without heatsinks, are tested to isolate the effect of the heatsinks on the performance of the TEH, as shown in Fig. 8(a). The outputs of both versions are measured across a 100 Ω load resistor, which is a close value to the internal resistance of the device. The output is measured through DrDAQ data loggers (from Pico Technology) connected to a laptop with a preinstalled application. The measurement is conducted for 24 h in the university campus starting at 12 pm. The output of the RFEH with heatsink antennas is recorded through the same measurement setup. The field test results are depicted in Fig. 8(b–c).

The RFEH with heatsink antennas harvests ∼250 mV across 10 kΩ and outperforms the previous version of the RFEH by 3 times in terms of collected energy for a 24 h period. The output of the RFEH is consistent throughout the whole day, with some spikes caused by nearby active users. As expected, this enhancement is attributed to the improvement in the radiation efficiency of

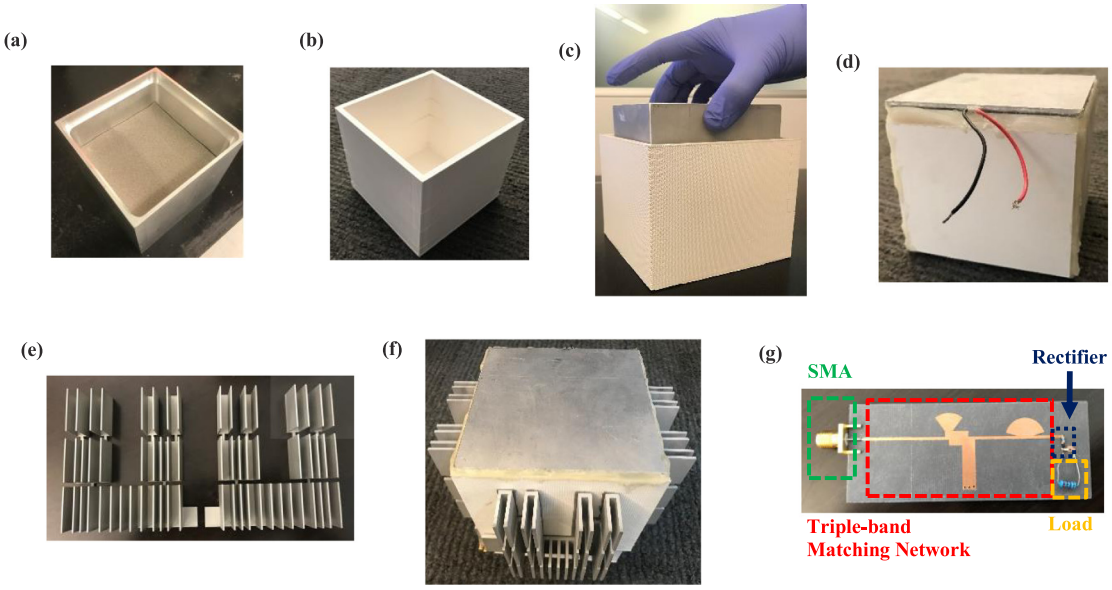

Fig. 7. (a) Outer ABS container (b) Al container filled with Ni foam (c) Intermediate step of placing the inner container inside the outer container (d) Fabricated TEH without heatsinks (e) Fabricated Al heatsink antenna (f) Fabricated TEH with heatsink antennas (g) Fabricated rectifier circuit with triple-band matching network.

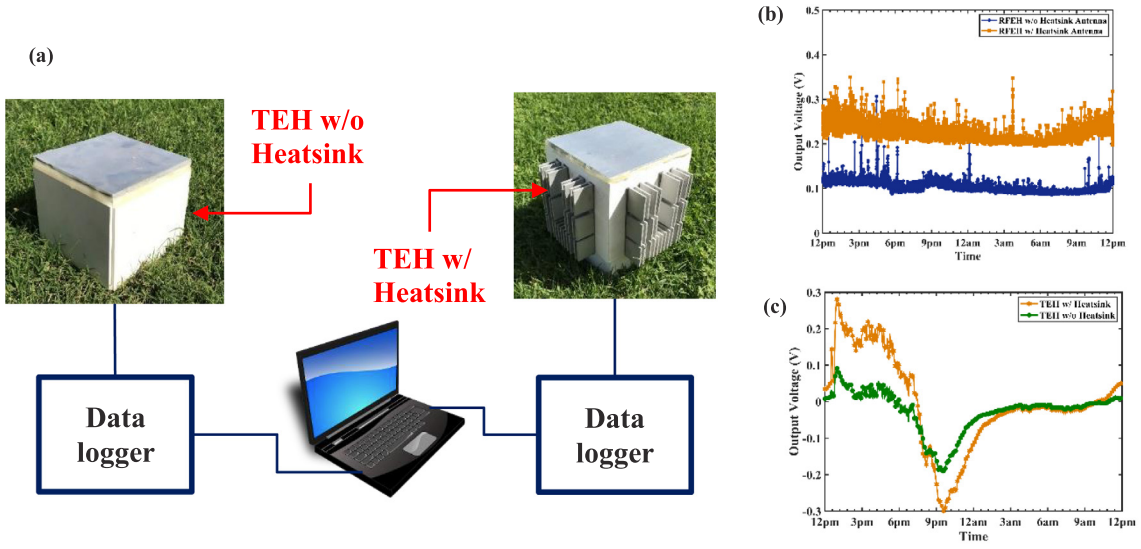

Fig. 8. (a) Field testing setup of the multi-source ambient energy harvester (b) Collected output voltage comparison for RFEH w/ and w/o heatsink antennas (c) Collected output voltage comparison for TEH w/ and w/o heatsink antennas.

the antenna when heatsink fins are integrated. Unlike the output of the RFEH, the output of the TEH is not constant; it follows the trend of the ambient environment temperature, as shown in Fig. 8(c). The figure shows that the output voltage (measured across 100 Ω) of the TEH with heatsinks is higher than that of the TEH without heatsinks because of the increased heat transfer. The energy collected by the TEH with heatsinks is 4 times that of the TEH without heatsinks. Energy is extracted by calculating the area under the curve of the power graph. Overall, the MSEH can collect 3680 μWh energy during 24 h field testing where 3530 μWh is generated by the TEH and the remaining 150 μWh is collected by the RFEH.

5. IoT application

The measurement setup for the demonstration of the synergistic MSEH in an IoT application is shown in Fig. 9(a). The environmental sensor CYALKIT-E02, which measures temperature and humidity, is used. The sensor node has a built-in BLE transceiver that is paired with a phone with a preinstalled Cypress application to visualize the received data. Because the output voltage of the ambient energy harvester is quite low (100–300 mV), the step-up converter TI BQ25504 is used to boost the output voltage to the required value of 2–3.3 V with 40% efficiency. A capacitor (1000 μF) is used to accumulate energy from the harvesters and power the environmental sensor. A parameter "time interval" is introduced to evaluate the average time required for a particular harvester to charge the sensor node with energy sufficient for one data transmission. To demonstrate the benefit of the multi-source RFEH and TEH with heatsink antennas, two scenarios are considered: the TEH or RFEH alone harvests energy and powers the environmental sensor. The recorded temperature and humidity data are presented in Fig. 9(b–c), which accurately represent the environmental conditions of the outdoor environment. As the TEH alone powers the sensor node, temperature and humidity data are acquired every 4.6 s; for the RFEH, the time interval is

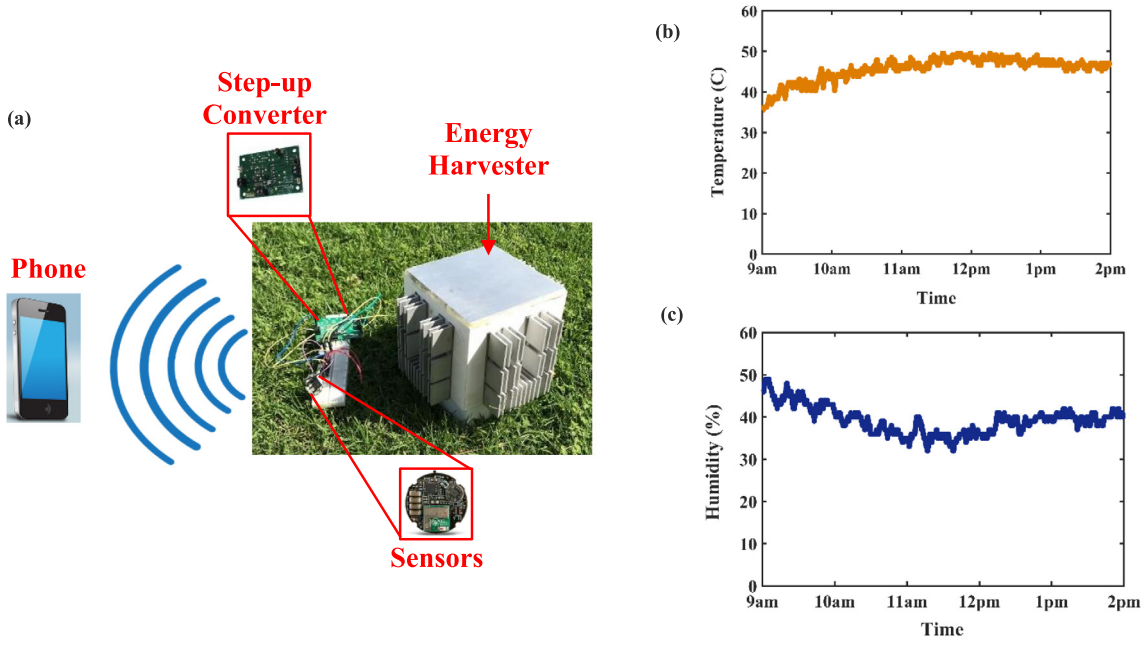

Fig. 9. (a) Measurement setup for IoT application (b) Environmental sensor readings of temperature (c) Environmental sensor readings of humidity.

58.5 s. These two values are within the reasonable range of the time interval for monitoring environmental variables. The time interval can be calculated if both the RFEH and the TEH are harvesting simultaneously. Energy collected in 24 h from the MSEH is 3680 μWh as mentioned in the previous section. Therefore, the time-averaged power collected from the MSEH is equal to 155 μW. Assuming power from two harvesters are combined with around ∼90% efficiency, the output power drops to 140 μW. The step-up converter used in the measurement has 40% efficiency which further decreases the output power to 56 μW. The datasheet of the BLE transceiver states that it requires 200 μJ of energy per one transmission. Thus, by dividing the energy consumption of the BLE to the output power of the MSEH, the time interval must reduce to each 3.5 s when both harvesters are active. These measurement results demonstrate the practicality of the ambient RFEH and TEH in future IoT applications and highlight the usefulness of the synergistic MSEH.

6. Conclusion

We presented a synergistic MSEH comprising an RFEH and a TEH. The TEH was in the shape of a box and utilized the heat leaked through the sidewalls via heatsinks. These heatsinks were co-optimized to operate as receiving antennas of the RFEH. With the use of this dual-function component, the performance of the TEH and the RFEH was enhanced by 4 and 3 times, respectively. During a 24 h field test, 3680 μWh energy was collected by the MSEH. IoT application was demonstrated by powering an environmental sensor measuring temperature and humidity using the MSEH.

CRediT authorship contribution statement

Azamat Bakytbekov: Conceptualization, Methodology, Formal analysis, Validation, Investigation, Writing. **Thang Q. Nguyen:** Conceptualization, Methodology, Formal Analysis, Validation. **Ge Zhang:** Conceptualization, Methodology, Formal analysis. **Michael S. Strano:** Conceptualization, Supervision. **Khaled N. Salama:** Conceptualization, Supervision. **Atif Shamim:** Conceptualization, Supervision.

Declaration of competing interest

The authors declare the following financial interests/personal relationships which may be considered as potential competing interests: Azamat Bakytbekov, Ge Zhang, Michael S Strano, Atif Shamim has patent #Multi-Source Ambient Energy Harvester, Nº 63/257,290, October 19, 2021. issued to US Patent and Trademark Office (USPTO).

Data availability

Data will be made available on request.

Acknowledgments

The research reported in this publication was supported by the King Abdullah University of Science and Technology (KAUST), Saudi Arabia. The authors acknowledge the KAUST Sensor Initiative, under award OSR-2015-Sensors-2700, for the financial support.

Special thanks go to Esraa Fakeih, who helped in collecting power measurement data on the KAUST campus.

References

Amoroso, Francesco, Pecora, Rosario, Ciminello, Monica, 2015. An original device for train bogie energy harvesting: a real application scenario. Smart Struct. Syst. 16 (3), 383–399.

Bakytbekov, Azamat, Nguyen, Thang Q., Huynh, Cuong, Salama, Khaled N., Shamim, Atif, 2018. Fully printed 3D cube-shaped multiband fractal rectenna for ambient RF energy harvesting. Nano Energy 53, 587–595.

Bakytbekov, A., Nguyen, T.Q., Li, W., Lee Cottrill, A., Zhang, G., Strano, M.S., Salama, K.N., Shamim, A., 2020. Multi-source ambient energy harvester based on RF and thermal energy: Design, testing, and IoT application. Energy Sci. Eng. 8, 3883.

Bakytbekov, A., Nguyen, T.Q., Zhang, G., Strano, M.S., Salama, K.N., Shamim, A., 2022. Dual-function triple-band heatsink antenna for ambient RF and thermal energy harvesting. IEEE Open J. Antennas Propag. 3, 263–273. http://dx.doi.org/10.1109/OJAP.2022.3149392.

Bakytbekov, A., Shamim, A., 2019. Additively manufactured triple-band fractal antenna-on-package for ambient RF energy harvesting. In: 2019 13th European Conference on Antennas and Propagation (EuCAP). pp. 1–3.

Balanis, C., 2005. Antenna Theory, Analysis and Design. Wiley, Hoboken, NJ.

Boisseau, S., Despesse, G., Seddik, B.A., 2012. Electrostatic conversion for vibration energy harvesting. In: Small-Scale Energy Harvesting. InTech, France, pp. 91–134.

Bowen, C.R., Arafa, M.H., 2015. Energy harvesting technologies for tire pressure monitoring systems. Adv. Energy Mater. 5 (7), 1401787.

Cheng, Fuqiang, Hong, Yanji, Li, Weiping, Guo, Xiaohong, Zhang, Hailong, Fu, Feng, Feng, Bingqing, Wang, Gang, Wang, Chao, Qin, Haibing, 2017. A thermoelectric generator for scavenging gas-heat: from module optimization to prototype test. Energy 121, 545–560.

Cho, Jae Yong, et al., 2016. Piezoelectric energy harvesting system with magnetic pendulum movement for self-powered safety sensor of trains. Sensors Actuators A 250, 210–218.

Cottrill, Anton L., Zhang, Ge, Tianxiang Liu, Albert, Bakytbekov, Azamat, Silmore, Kevin S., Koman, Volodymyr B., Shamim, Atif, Strano, Michael S., 2019. Persistent energy harvesting in the harsh desert environment using a thermal resonance device: Design, testing, and analysis. Appl. Energy 235, 1514–1523.

Deng, F., Yue, X., Fan, X., Guan, S., Xu, Y., Chen, J., 2019. Multi-source energy harvesting system for a wireless sensor network node in the field environment. IEEE Internet Things J. 6 (1), 918–927. http://dx.doi.org/10.1109/JIOT.2018.2865431.

Evans, J.W., Kim, B., Ono, S., Arias, A.C., Wright, P.K., 2021. Multicycle testing of commercial coin cells for buffering of harvested energy for the IoT. IEEE Internet Things J. 8 (12), 10047–10051. http://dx.doi.org/10.1109/JIOT.2021.3050735.

Fathabadi, H., 2018. Internal combustion engine vehicles: Converting the waste heat of the engine into electric energy to be stored in the battery. IEEE Trans. Veh. Technol. 67 (10), 9241–9248. http://dx.doi.org/10.1109/TVT.2018.2854876.

Guo, L., Gu, X., Chu, P., Hemour, S., Wu, K., 2020. Collaboratively harvesting ambient radiofrequency and thermal energy. IEEE Trans. Ind. Electron. 67 (5), 3736–3746. http://dx.doi.org/10.1109/TIE.2019.2914627.

He, W., Shi, W., Le, J., Li, H., Ma, R., 2020. Geophone-based energy harvesting approach for railway Wagon monitoring sensor with high reliability and simple structure. IEEE Access 8, 35882–35891. http://dx.doi.org/10.1109/ACCESS.2020.2968089.

Hu, Youfan, Xu, Chen, Zhang, Yan, Lin, Long, Snyder, Robert L., Wang, Zhong Lin, 2011. A nanogenerator for energy harvesting from a rotating tire and its application as a self-powered pressure/speed sensor. Adv. Mater. 23 (35), 4068–4071.

Incropera, F.P., 2007. Heat transfer from extended surfaces. In: Fundamentals of Heat and Mass Transfer, sixth ed. John Wiley & Sons, US.

Jeon, Seung-Bae, Kim, Daewon, Yoon, Gun-Wook, Yoon, Jun-Bo, Choi, Yang-Kyu, 2015. Self-cleaning hybrid energy harvester to generate power from raindrop and sunlight. Nano Energy 12, 636–645.

Lee, Jaeyun, Choi, Bumkyoo, 2014. Development of a piezoelectric energy harvesting system for implementing wireless sensors on the tires. Energy Convers. Manage. 78, 32–38.

Lee, W.-K., Schubert, M.J.W., Ooi, B.-Y., Ho, S.J.-Q., 2018. Multi-source energy harvesting and storage for floating wireless sensor network nodes with long range communication capability. IEEE Trans. Ind. Appl. 54 (3), 2606–2615. http://dx.doi.org/10.1109/TIA.2018.2799158.

Li, Yongliang, Witharana, Sanjeeva, Cao, Hui, Lasfargues, Mathieu, Huang, Yun, Ding, Yulong, 2014. Wide spectrum solar energy harvesting through an integrated photovoltaic and thermoelectric system. Particuology 15, 39–44.

Li, X., et al., 2021. ViPSN: A vibration-powered IoT platform. IEEE Internet Things J. 8 (3), 1728–1739. http://dx.doi.org/10.1109/JIOT.2020.3016993.

Liu, Y., Voigt, T., Wirström, N., Höglund, J., 2019. EcoVibe: On-demand sensing for railway bridge structural health monitoring. IEEE Internet Things J. 6 (1), 1068–1078. http://dx.doi.org/10.1109/JIOT.2018.2867086.

Lorenz, C.H.P., Hemour, S., Liu, W., Badel, A., Formosa, F., Wu, K., 2015. Hybrid power harvesting for increased power conversion efficiency. IEEE Microw. Wirel. Compon. Lett. 25 (10), 687–689. http://dx.doi.org/10.1109/LMWC.2015.2463229.

Ni, Z., Bhat, R.V., Motani, M., 2018. On dual-path energy-harvesting receivers for IoT with batteries having internal resistance. IEEE Internet Things J. 5 (4), 2741–2752. http://dx.doi.org/10.1109/JIOT.2018.2813976.

Nishijima, Yoshiaki, Komatsu, Ryosuke, Yamamura, Takuya, Balčytis, Armandas, Seniutinas, Gediminas, Juodkazis, Saulius, 2017. Design concept of a hybrid photo-voltaic/thermal conversion cell for mid-infrared light energy harvester. Opt. Mater. Express 7 (10), 3484–3493.

Orr, Bradley, Akbarzadeh, Aliakbar, Mochizuki, Masataka, Singh, Randeep, 2016. A review of car waste heat recovery systems utilising thermoelectric generators and heat pipes. Appl. Therm. Eng. 101, 490–495.

Ramson, S.R.J., et al., 2021. A self-powered, real-time, LoRaWAN IoT-based soil health monitoring system. IEEE Internet Things J. 8 (11), 9278–9293.

Risseh, A.E., Nee, H., Goupil, C., 2018. Electrical power conditioning system for thermoelectric waste heat recovery in commercial vehicles. IEEE Trans. Transp. Electrif. 4 (2), 548–562. http://dx.doi.org/10.1109/TTE.2018.2796031.

Sadeqi, S., Arzanpour, S., Hajikolaei, K.H., 2015. Broadening the frequency bandwidth of a tire-embedded piezoelectric-based energy harvesting system using coupled linear resonating structure. IEEE/ASME Trans. Mechatronics 20 (5), 2085–2094. http://dx.doi.org/10.1109/TMECH.2014.2362685.

Shim, Y., Park, H., Shin, W., 2021. Joint time allocation for wireless energy harvesting decode-and-forward relay-based IoT networks with rechargeable and nonrechargeable batteries. IEEE Internet Things J. 8 (4), 2792–2801. http://dx.doi.org/10.1109/JIOT.2020.3020960.

Singh, Kanwar Bharat, Bedekar, Vishwas, Taheri, Saied, Priya, Shashank, 2012. Piezoelectric vibration energy harvesting system with an adaptive frequency tuning mechanism for intelligent tires. Mechatronics 22 (7), 970–988.

Statista Research Department, 2019. Internet of Things - Number of Connected Devices Worldwide 2015–2025. 2019. https://www.statista.com/statistics/471264/iot-number-of-connected-devices-worldwide/.

Tan, Y.K., Panda, S.K., 2011. Energy harvesting from hybrid indoor ambient light and thermal energy sources for enhanced performance of wireless sensor nodes. IEEE Trans. Ind. Electron. 58 (9), 4424–4435. http://dx.doi.org/10.1109/TIE.2010.2102321.

Temizer, İlker, İlkılıç, Cumali, 2016. The performance and analysis of the thermoelectric generator system used in diesel engines. Renew. Sustain. Energy Rev. 63, 141–151.

Virili, Marco, Georgiadis, Apostolos, Collado, Ana, Niotaki, Kyriaki, Mezzanotte, Paolo, Roselli, Luca, Alimenti, Federico, Carvalho, Nuno, 2015. Performance improvement of rectifiers for WPT exploiting thermal energy harvesting. Wirel. Power Transf. 2, 1–10. http://dx.doi.org/10.1017/wpt.2015.4.

Wang, Yingli, Duan, Jialong, Duan, Yanyan, Zhao, Yuanyuan, Pang, Zhibin, He, Benlin, Tang, Qunwei, 2017. Interfacial engineering of hybridized solar cells for simultaneously harvesting solar and rain energies. J. Mater. Chem. A 5 (35), 18551–18560.

Yi, Z., Yang, B., Zhang, W., Wu, Y., Liu, J., 2021. Batteryless tire pressure real-time monitoring system driven by an ultralow frequency piezoelectric rotational energy harvester. IEEE Trans. Ind. Electron. 68 (4), 3192–3201. http://dx.doi.org/10.1109/TIE.2020.2978727.

Zhang, L., Chin, K.-W., Wang, L., Yang, C., 2022. Complete targets coverage in energy harvesting IoT networks with dual imperfect batteries. IEEE Internet Things J. http://dx.doi.org/10.1109/JIOT.2021.3109148.

Zhang, Hulin, Zhang, Shangjie, Yao, Guang, Huang, Zhenlong, Xie, Yuhang, Su, Yuanjie, Yang, Weiqing, Zheng, Chunhua, Lin, Yuan, 2015. Simultaneously harvesting thermal and mechanical energies based on flexible hybrid nanogenerator for self-powered cathodic protection. ACS Appl. Mater. Interfaces 7 (51), 28142–28147.

Zheng, Li, Lin, Zong-Hong, Cheng, Gang, Wu, Wenzhuo, Wen, Xiaonan, Lee, Sangmin, Wang, Zhong Lin, 2014. Silicon-based hybrid cell for harvesting solar energy and raindrop electrostatic energy. Nano Energy 9, 291–300.

Zhong, Huikai, Wu, Zhiqian, Li, Xiaoqiang, Xu, Wenli, Xu, Sen, Zhang, Shengjiao, Xu, Zhijuan, Chen, Hongsheng, Lin, Shisheng, 2016. Graphene based two dimensional hybrid nanogenerator for concurrently harvesting energy from sunlight and water flow. Carbon 105, 199–204.

Mr. Azamat Bakytbekov received his bachelor's degree from the Electrical Engineering and Electronics Department at Nazarbayev University in Kazakhstan in 2015, and his master's degree from the Electrical Engineering Department at King Abdullah University of Science and Technology (KAUST) in 2017. He is currently Ph.D. student at KAUST under supervision of Dr. Atif Shamim. His research interests include multiband and wideband printed antennas, printed electronics, RF energy harvesters and multi-source energy harvesters.

Thang Q. Nguyen received the B.E. degree in telecommunication engineering from Ho Chi Minh University of Technology (HCMUT), Ho Chi Minh City, Vietnam in 2017.

He joined the Sensors Lab at KAUST, Saudi Arabia as a visiting student in summer 2017 where he conducted research on multi-band RF energy harvesting systems. He is currently a master student at KAUST. His research focus on RF energy harvesting systems and Wireless sensor systems.

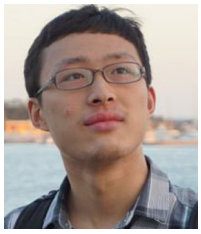

Ge Zhang received his bachelor's degree in chemical engineering in 2017 from Tsinghua University. He is currently a Ph.D. student in Prof. Michael Strano's lab at Massachusetts Institute of Technology. His research interests include novel energy harvesting systems such as thermal resonator, and building power sources to enable the independent operation of cell-sized micro-electronic systems dispersed in environment.

Michael S. Strano is currently the Carbon P. Dubbs Professor in the Chemical Engineering Department at the Massachusetts Institute of Technology. His research focuses on biomolecule/nanoparticle interactions and the surface chemistry of low dimensional systems, nanoelectronics, nanoparticle separations, and applications of vibrational spectroscopy to nanotechnology.

Dr. Salama received his masters and doctorate degrees from the Electrical Engineering Department at Stanford University. His work on CMOS sensors for molecular detection was awarded the Stanford-Berkeley Innovators Challenge Award in biological sciences and was acquired by Lumina Inc in 2008. He was an assistant professor at RPI between 2005 and 2008. He is a Professor and founding chair member in the Electrical engineering department at King Abduallah University of Science and Technology. He is currently the director of the sensor initiative at KAUST. He is the co-author of 200 papers and 14 patents on sensors.

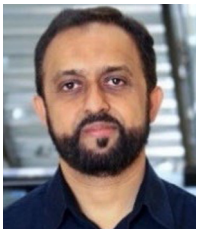

Atif Shamim received M.S. (2004) and Ph.D. degrees (2009) in electrical engineering from Carleton University, Canada. In 2010, he joined KAUST and is currently an Associate Professor. His research work has won several best paper awards in prestigious conferences and has been highlighted in international media. He has won numerous awards, OCRI Researcher of the Year (2008), OCRI Entrepreneur of the year (2010), 1st prize in CMC Competition (2007) and 1st prize in Canada's national business plan competition (2009). He is an author of 200 international publications, inventor on 20 patents and has given 40 invited talks at international forums.